Article

Graphene Thermal Infrared Emitters Integrated into Silicon Photonic Waveguides

Nour Negm, Sarah Zayouna, Shayan Parhizkar, Pen-Sheng Lin, Po-Han Huang, Stephan Suckow, Stephan Schroeder, Eleonora De Luca, Floria Ottonello Briano, Arne Quellmalz, Georg S. Duesberg, Frank Niklaus, Kristinn B. Gylfason, and Max C. Lemme*

Read Online

ACCESS | Metrics & More | Article Recommendations | SI Supporting Information

ABSTRACT: Cost-efficient and easily integrable broadband mid-infrared (mid-IR) sources would significantly enhance the application space of photonic integrated circuits (PICs). Thermal incandescent sources are superior to other common mid-IR emitters based on semiconductor materials in terms of PIC compatibility, manufacturing costs, and bandwidth. Ideal thermal emitters would radiate directly into the desired modes of the PIC waveguides via near-field coupling and would be stable at very high temperatures. Graphene is a semimetallic two-dimensional material with comparable emissivity to thin metallic thermal emitters. It allows maximum coupling into waveguides by placing it directly into their evanescent fields. Here, we demonstrate graphene mid-IR emitters integrated with photonic waveguides that couple

directly into the fundamental mode of silicon waveguides designed to work in the so-called "fingerprint region" relevant for gas sensing. High broadband emission intensity is observed at the waveguide-integrated graphene emitter. The emission at the output grating couplers confirms successful coupling into the waveguide mode. Thermal simulations predict emitter temperatures up to 1000 °C, where the blackbody radiation covers the mid-IR region. A coupling efficiency η, defined as the light emitted into the waveguide divided by the total emission, of up to 68% is estimated, superior to data published for other waveguide-integrated emitters.

KEYWORDS: graphene, thermal emitter, mid-infrared, optical gas sensing, absorption spectroscopy, silicon photonics
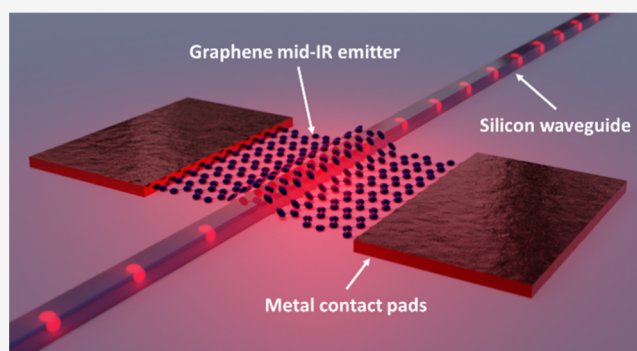
INTRODUCTION

The demand for distributed, networked, and compact gas sensors[1−4] for real-time air quality monitoring is rapidly increasing in a wide range of applications such as demand-controlled ventilation in heating and air conditioning (HVAC) systems,[5,6] gas leak detection,[7] industrial process control,[8,9] environmental monitoring[10−12] and medical diagnostics.[13] Typical gas sensing methods are often based on chemical reaction sensors such as catalytic beads or electrochemical and semiconducting metal oxides.[1,4] In these types of sensors, the targeted gas undergoes a chemical reaction with the sensor material and thus alters the sensor itself. This leads to drift over time, the need for frequent calibration, performance degradation, and a limited sensor lifetime. Absorption spectroscopy, in contrast, exploits the fundamental absorption lines of trace and greenhouse gases in the mid-infrared (mid-IR) region. This allows "fingerprinting" the gases through characteristic absorption wavelengths between 3 and 10 μm, e.g., carbon dioxide (CO_2) at 4.2 μm.[14] Thus, absorption spectroscopy is an optical gas sensing technology that provides high specificity,

minimal drift, and long-term stability without chemically altering the sensor.[2,3]

Photonic integrated circuits (PICs) enable shrinking spectroscopy equipment to the size of a chip, resulting in highly miniaturized and cost-efficient optical gas sensor systems. However, recent work demonstrating PIC-based gas sensors still requires light coupling from external sources and to detectors into and out of the waveguides, respectively.[15−17] Integrating these components directly on the wafer level would reduce the sensor system size and cost, enhance mechanical stability, and potentially enhance performance, thus enabling the widespread use of such systems as air quality monitors. There is promising progress for waveguide-integrated mid-IR
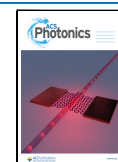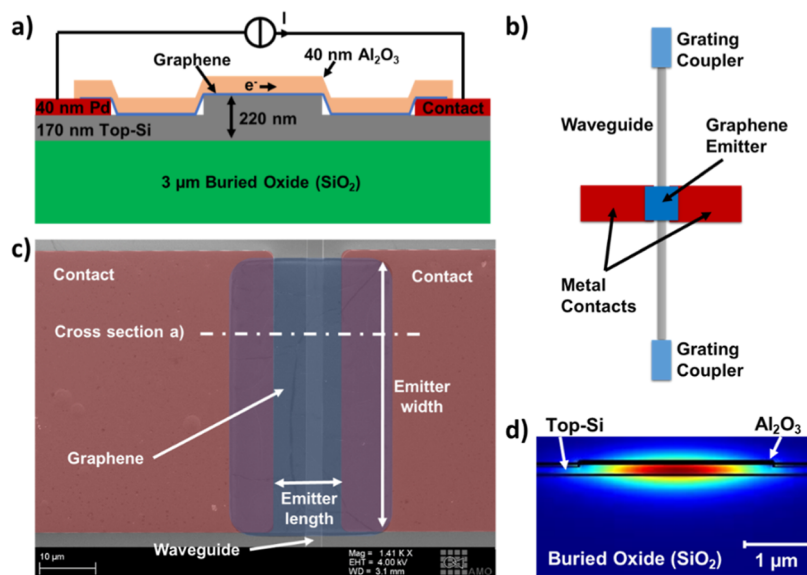
Figure 1. Device layout and waveguide simulation. (a) Schematic cross-section of the graphene waveguide-integrated thermal emitter after encapsulation. The electrical connection scheme illustrates the Joule heating method to generate thermal emissions. (b) Schematic top view of the components of the PIC. (c) False-colored scanning electron micrograph before encapsulation. (d) Simulated electric field profile of the fundamental TE mode of the waveguide, including relevant materials.

photodetectors (including graphene and other 2D materials),[18−25] but the realization of waveguide-integrated mid-IR emitters has seen very limited success to date. Commonly used mid-IR emitting materials such as small bandgap III−V or II−VI semiconductor compounds cannot easily be integrated with CMOS and PIC substrates because of their fabrication processes and high thermal budgets. They also suffer from high manufacturing costs due to their complex epitaxial multilayer systems, and their light emission has a limited bandwidth, making them unsuitable for compact multigas sensor applications requiring broadband emission.[26−30]

Alternatively, thermal incandescent light sources are well-established and cost-effective mid-IR sources. They work by Joule heating realized by forcing an electric current through the emitter material, causing broadband thermal blackbody emission according to Planck's law. The precise spectral distribution of the emitted radiation depends mainly on the temperature of the emitter, but it is, in any case, broadband. The design of thermal incandescent sources is comparably simple, as they are generally composed of a layer of an electrically conductive emitting material and two electrical contact pads. Such emitters can be integrated on-chip with optoelectronic components and PICs in high-volume production flows. The latter enables near-field coupling of their emission directly into the waveguided modes. Graphene is an excellent candidate for such emitters, as it has been shown to reach the required temperatures for thermal emission in the mid-IR.[31] Its emissivity is also comparable to that of other very thin emitters.[32,33] At the same time, monolayers of graphene are so thin that the entire emitting volume can be placed closest to the waveguide, generating ideal near-field coupling. Thicker metallic emitters partly shield their own radiation. Finally, monolayer graphene only minimally distorts the waveguided mode, which minimizes the mismatch between the mode in the emitter region and outside this region.

In this work, we show a waveguide-integrated incandescent thermal mid-IR emitter that uses graphene as the active material. We experimentally demonstrate graphene emitters integrated directly on top of silicon photonic waveguides. The emitters couple directly into the waveguide mode. We detect emissions in the spectral range of 3 to 5 μm.

■ RESULTS

Device Layout and Waveguide Simulation. A sketch of the cross-section, a schematic top view, and a scanning electron microscope (SEM) image of our waveguide-integrated emitters are shown in Figure 1a−c. The thermal emitter mainly consists of a graphene sheet on top of the Si waveguide, with contacts on each side. A layer of Al_2O_3 was used to encapsulate the graphene from the environment (Methods). Two grating couplers are included to outcouple radiation at each end of the waveguides. The fundamental quasi-TE mode profile in the waveguides calculated for λ = 4.2 (Methods) is shown in Figure 1d.

Mid-IR Setup and Measurements. Two probe needles were used to contact the graphene emitters via the metal pads with a source measure unit (SMU), which acted as a DC current source and voltage meter simultaneously (Figure 2a). A DC current was forced into the emitters starting at 5 mA and ramped up to 25 mA in incremental steps of 0.2 mA for 5 s, and the voltage drop across the emitters was monitored. In addition, we captured top-view IR images of the devices with an infrared camera with a spectral wavelength range from 3 to 5 μm. The camera was positioned above the chip to detect the light emitted at the emitter and one of the two grating couplers at the end of the waveguide. All measurements were conducted in an ambient atmosphere with 10 to 20% humidity at 22 °C.

An IR image of a waveguide-integrated graphene emitter operated at a current density of 0.45 mA/μm (current normalized to graphene channel width), corresponding to a power of 185 mW, is shown in Figure 2b. Mid-IR emission is visible both at the graphene emitter and at the output grating coupler. The emission at the grating couplers clearly demonstrates that the graphene emits IR radiation, which is then coupled into and propagates through the waveguide to the grating couplers. This proves the functionality of the
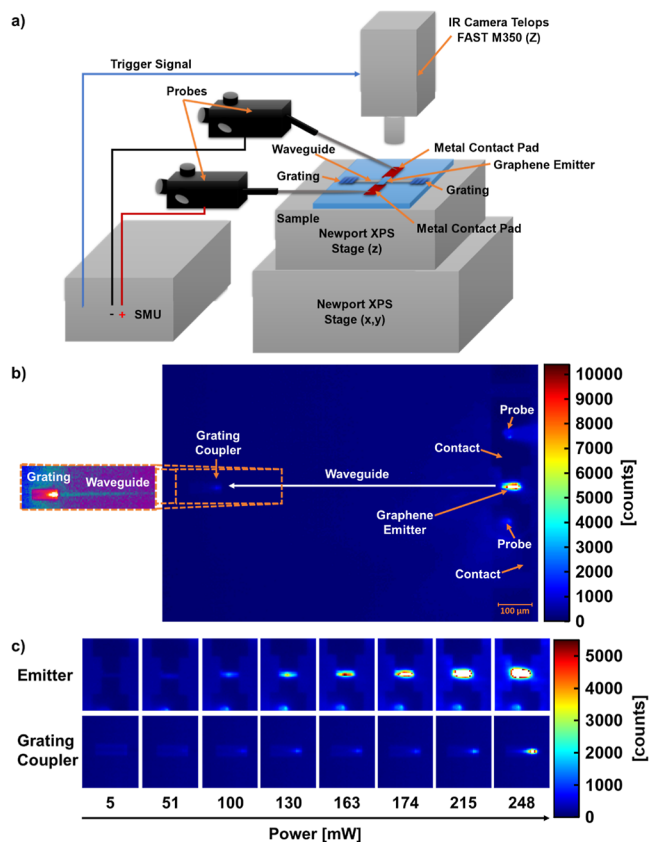
Figure 2. Mid-IR setup and measurements. (a) Schematic of the mid-IR measurement setup, showing the components and connections to the integrated thermal emitter on the sample. In (b,c) the camera focuses on the emitter and one of the output grating couplers. (b) Mid-IR camera image of a thermal emitter operated at 185 mW. The emitter, contact pads, and probes are visible on the right. The waveguide output grating coupler is visible on the left. The length of the waveguide between the grating coupler and emitter is 725 μm. Inset: Extraction of the output grating with enhanced contrast (using a different color scale), to visualize the radiation pattern of the outcoupled light and the scattering from the waveguide. The scale bar is valid for the entire (b). (c) Mid-IR camera images of the emitter and grating coupler from (b), at different power levels.

graphene emitter and its successful integration with the photonic waveguide. The sequence of images in Figure 2c illustrates the power dependency of the emission. Note that additional emission visible at the probe tips is due to reflections of the emitted light. This is therefore disregarded in the following analysis.

The emission intensity at the output grating coupler is significantly lower than at the emitter. There are several reasons for this. First, the graphene emitter exhibits a typical gray body broadband emission, which the IR camera partly captures in the wavelength range from 3 to 5 μm. However, the grating couplers are wavelength-selective and filter out some of the broadband radiation coming from the emitter (details in Supporting Information SI1 and SI2). Second, the emitter-waveguide coupling is not perfect and leads to losses, as well as waveguide propagation losses. We measured the waveguide propagation losses at λ = 4.2 μm with the cutback method and obtained 14.6 ± 3.5 dB/cm (details in Supporting Information SI1). This value is close to the intrinsic waveguide propagation loss of 13.7 dB/cm, calculated with the Ansys Lumerical Mode Solver. As expected, the simulation underestimates the loss

because the model only includes absorption in the BOx layer but not scattering losses. The device shown in Figure 2, with its length of 725 μm thus contributes a total waveguide propagation loss of approximately 1 dB.

Emitter Coupling Efficiency. We estimated the coupling efficiency η of the emitter from the camera images as shown in Figure 2. η is defined as the intensity of the light emitted from the emitter into the waveguide $I_{E,in}$, divided by the total emissions of the emitter, $\eta = I_{E,in}/(I_{E,out} + I_{E,in})$, with $I_{E,out}$ being the emission intensity extracted above the emitter by the camera. First, the background illumination level was subtracted in each image using an off-state IR image of the area under investigation. Then, the emission intensity at the grating coupler $I_{GC,out}$ and at the emitter $I_{E,out}$ was extracted by integrating the camera counts around the respective emission peak positions. Note that we are using counts for convenience, but this is not raw data but data calibrated for linearity (we go into more detail about the different IR camera calibration modes used in this paper and our current analysis limitations in Supporting Information SI3). We defined the emission area as the set of pixels with more counts than $1/e$ of the peak value. The emission intensity was $I_{GC,out} = 9154$ counts at the grating coupler and $I_{E,out} = 230{,}990$ counts at the emitter based on the image in Figure 2b. Although this methodology excludes photons interacting with the surface or emitted at angles outside of the numerical aperture of the camera, we expect this data to be at least sufficient for calculating an apparent coupling efficiency. Next, to calculate $I_{E,in}$ from $I_{GC,out}$, we considered the optical losses of the waveguide and the grating coupler. We used the measured waveguide loss of 1 dB (i.e., an efficiency of 80% = 0.8), assuming that the propagation loss measured at 4.2 μm is representative of the entire wavelength range captured by the camera (3−5 μm). Making the same assumption for the optical losses of the grating coupler is not possible due to the strong spectral filtering of the grating. We, therefore, extended the simulation of the grating coupler efficiency to include the camera's sensitivity range (see Supporting Information SI2) and obtained an average value of approximately 23% = 0.23. We further assumed symmetrical emission into each side of the waveguide, adding a factor of 2 to the calculation. The emission into the waveguide can then be calculated to $I_{E,in} = 2I_{GC,out}/0.8/0.23 = 99{,}500$ counts, and the efficiency of the emitter was calculated to be $\eta = 30\%$.

The measured emission intensities of the graphene emitter and output grating coupler and the coupling efficiency of the emitter are plotted as a function of electrical power in Figure 3. The intensities at the grating coupler and emitter start to distinctly stand out from the background at a power of approximately 40 to 50 mW, in line with the camera images in Figure 2c. The efficiency calculation should therefore be disregarded below this value, as the data widely fluctuates (grayed out). Over 50 mW, the efficiency is between 55 and 65%, with a maximum of 68% at 123 mW. It then decreases to around 40% in the power range of 150 to 174 mW and around 30% as the emitter starts exhibiting signs of a thermal runaway, i.e. overheating beyond repair, at 185 mW. The efficiency increases again to 40% and then over 80% just as the device breaks down.

The internal efficiency of the system, $\eta = I_{GC,out}/(I_{E,out} + I_{GC,out})$, shows a similar progression as the calculated emitter-to-waveguide coupling efficiency, with a maximum of 17% at a power of 123 mW. However, since our work focuses on the efficiency of the graphene emitter coupling into the waveguide
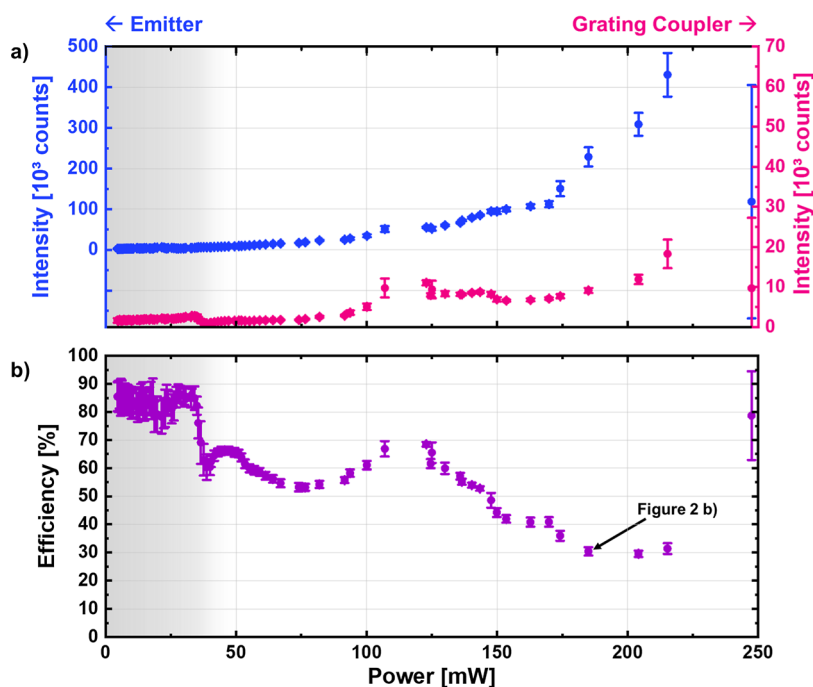
Figure 3. Emission efficiency. (a) Mean and standard deviation of the emission intensities of the graphene emitter and output grating coupler as a function of DC electric power extracted from IR images as illustrated in Figure 2. The IR camera recorded 50 frames per current increment. The two data sets are offset for clarity. (b) Calculated coupling efficiency of the graphene emitter (mean and standard deviation) as a function of electric power.
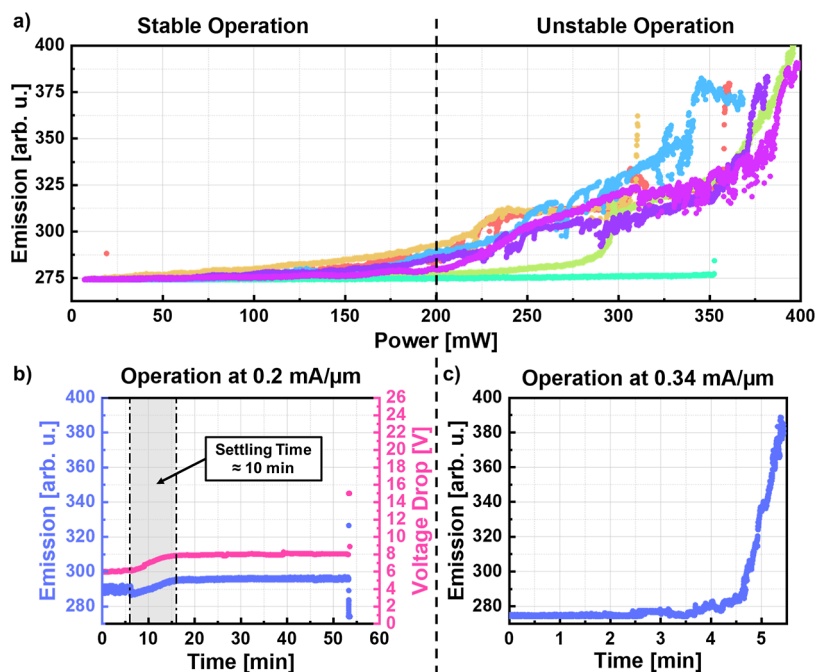

Figure 4. Operating regimes and stability. (a) Emission in arbitrary units (arb. u.)—as extracted from the IR camera software—of seven nominally identical emitters vs input power. (b) Emission in arbitrary units and voltage drop of an emitter driven in the stable regime with 0.2 mA/μm, corresponding to 60−80 mW, vs time. (c) Emission in arbitrary units of an emitter driven in the unstable regime with 0.34 mA/μm vs time.

rather than the internal efficiency of the entire optical system of the emitter, waveguide, and grating coupler, we are providing this only as Supporting Information SI4.

Wien's displacement law offers a qualitative explanation of the measured efficiency decrease with heating power, i.e., emitter temperature. The law states that high temperatures shift the peak emission of the thermal emitter to shorter

wavelengths. The free space emission at the emitter side, however, is not affected by this spectral change. The camera captures all radiation in the waveband of 3 to 5 μm within the numerical aperture of the objective, which translates to an angle of 26.5°. However, the emission at the grating coupler is expected to vary from an angle of −20° at 5 μm wavelength to 40° at 3 μm wavelength. Therefore, the shortest wavelength
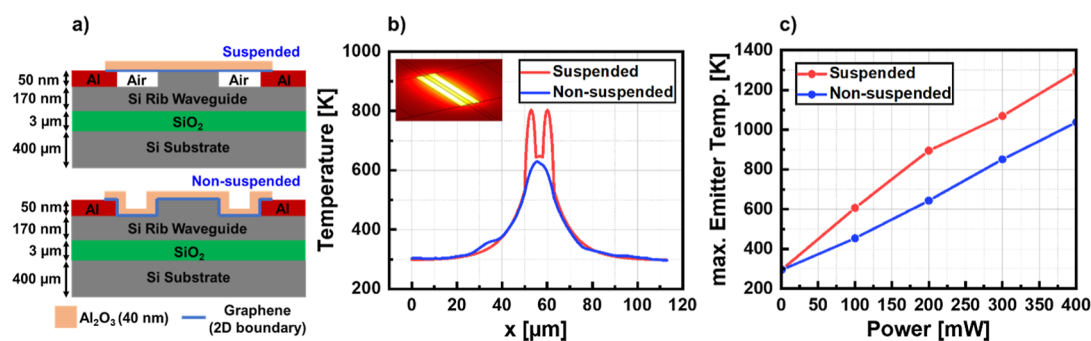
Figure 5. Electro-thermal simulation. (a) Schematic of the two electro-thermal model configurations used to predict the temperature of the graphene emitters. (b) Simulated temperature distribution of the graphene sheets vs position perpendicular to the waveguide at 185 mW power supply. (c) Simulated maximum temperature of the graphene emitters vs power.

Table 1. Comparison of the Present Work (Highlighted in Green) with the State-Of-The-Art[a]

Ref.	Material	Coupled to	Est. Coupling Efficiency	Current / Current Density	Voltage	Power Cons. / Power Density	Emitting Area	Temperature	Lifetime
Here	Graphene monolayer	Waveguide	28 – 68%	10 – 27 mA 0.2 – 0.45 mA/μm	6 – 18 V	60 – 200 mW 0.12 – 0.4 mW/μm²	50 x 10 μm²	500 – 900 K*	> 54 min
34,35	Kanthal (FeCrAl)	Free space		150 – 200 mA	6.5 V	0.8 – 1 W 0.8 – 1 W/mm²	1 x 1 mm²	700 – 1200 K	
34,36	Pt Nanowire	Free space				5 mW 2.9 mW/μm²	3.5 μm x 500 nm	595 K	
31	Graphene	Free space		1 – 2 x10⁸ A/cm²	16 – 21 V	~ 80 kW/cm²		1600 K	
32	Graphene multilayer	Free space			8 V			750 K*	> 1000 h
45	CNT (3 – 100 μm⁻¹)	Waveguide	45 – 55%		1.5 – 10 V_DC & additional 2 – 3.3 V_pulse			1000 – 1500 K*	
46	NCG (5 nm thick, ~15 layers)	Waveguide	84 – 99%*	70 μA	41 V	2.87 mW 5.74 mW/μm²	~ 250 nm x 2 μm	1000 K	

[a]The most relevant values used for comparison are highlighted in yellow. Simulated values are marked by *. CNT = carbon nanotube. NCG = nanocrystalline graphene.

emission is not collected by the objective (see Supporting Information SI5). The fraction of emission at 3 μm wavelength increases with increasing emitter temperature, leading to an apparent drop in coupling efficiency measured by our camera. We attempt a more quantitative explanation of the estimated efficiency progression with heating power in Supporting Information SI6.

Operating Regimes and Stability. We further explored the potential operating regimes and stability of the emitters. Figure 4a shows the emitter emission as a function of DC electric power for seven nominally identical emitters. Two operating regimes can be identified. There is stable operation below a power threshold of approximately 200 mW and unstable operation characterized by fluctuations and thermal runaway between 250 and 350 mW before final breakdown at different power levels.

Figure 4b shows the emission of and the voltage drop along one device operated in the stable regime with a constant current of 0.2 mA/μm over time. The device was operated continuously for a total of 54 min. After an initial stable plateau for the first 6 min, we observed an increase in emission and voltage over 10 min. The voltage change originates from a resistance change of the emitter, which may be attributed to current-induced damage to parts of the graphene sheet or the graphene-metal contacts, which increased the total resistance of the emitter and thus the heating power (here: from 60 to 80 mW). Afterward, the device was stable for 40 min before the measurements were terminated. Another device was operated at a current density of 0.34 mA/μm. Although the voltage drop across this device was not measured, we consider it to be in the

unstable operating regime based on typical average resistances of the graphene sheets. This device remained stable for only 2.5 min, after which the emission started to increase in a thermal runaway until the device broke down after 5.4 min. The thermal runaway is expected to be initiated by local current-induced defects in the graphene, which increase the resistance and, as the supplied current is constant, increase the heating power. This causes more defects, even higher heating power and, eventually, breakdown. The resulting enhanced emission comes at the price of defect generation and, ultimately, device failure.

Electro-Thermal Simulation. The electro-thermal behavior of the emitters was further investigated with finite element simulations using COMSOL Multiphysics software (see Methods section). Two different device configurations were modeled, (1) one where the graphene sheet is suspended and only supported by the metal pads and the silicon waveguide, and (2) one where the graphene adheres completely to the topography of the metal pads, the silicon waveguide, and the substrate (see schematics in Figure 5a). In the actual devices, the graphene sheet is assumed to be in a configuration between those two model configurations (compare Figure 1a). The simulated temperature distributions of the emitters at a power supply of 185 mW, which corresponds to the experimental data in Figure 2b, are shown in Figure 5b. The maximum temperature of the suspended graphene sheet is 803 K, while the graphene that is supported by the Si reaches a temperature of 629 K. The maximum value of the former is located at the centers of the two suspended regions, where the cooling by the environment is the weakest. The fully supported graphene is

cooled more efficiently through contact with the substrate and reaches its maximum temperature at the center of the waveguide. The two "hot spots" of the suspended emitter make this configuration more efficient as a light source, as the power emitted by a blackbody scales with the fourth power of the temperature. However, this configuration also increases the risk of thermal runaway and breakdown, which mostly happened in our case near the contact edges and the edges of the waveguides (see Supporting Information SI7).

The simulations in Figure 5c show that both emitter types reach temperatures well over 500 K in the stable experimental operating regime. This corresponds to blackbody radiation that sufficiently covers the mid-IR region. These theoretical results confirm that our graphene waveguide-integrated thermal emitters are suitable mid-IR sources.

◼ DISCUSSION

Table 1 compares the performance of our graphene emitters with the current state of the art achieved with both conventional materials and other nanoemitters. We included representative publications of thick and thin metallic thermal emitters emitting into free space.[34−36] We also covered publications on thermal graphene emitters emitting into free space[31−33,37−40] and representative publications for monolayer and multilayer graphene. We extended the list to incandescent emitting materials,[41−45] which includes electroluminescent and incandescent CNT emitters coupled with photonic waveguides. Finally, we added a very recent publication on an electroluminescent CNT emitter coupling into a photonic crystal (PhC) cavity on a photonic waveguide,[46] which also includes a similar design with nanocrystalline graphene (NCG) that shows incandescent light emission.

Our devices reach comparable temperatures, the most crucial parameter for thermal emitters. Our graphene emitters further have advantages over the metallic emitters in terms of power consumption and emission area, as they can be directly integrated on top of waveguides and in larger areas without the typical trade-off with reabsorption losses caused by the emitting material (assuming perfect transparency of graphene). The estimated coupling efficiency in the range of 28 to 68% of our graphene emitters compares well with the published CNT emitter,[45] even if optical propagation losses and scattering of other wavelengths from the grating coupler were neglected there, which could increase the estimated efficiency by several percent. Nevertheless, graphene emitters would still be favorable, considering the more challenging fabrication processes needed for CNTs, especially on wafer-scale.[47] The waveguide-integrated incandescent NCG emitters showed high power density,[46] which we attribute to their condensed size and high temperature. However, the calculation of the coupling efficiency is not comparable to our devices. It is unclear if the reported efficiencies are simulated or calculated from experimental data. Finally, our work provides wafer-scale graphene transfer and conventional stepper lithography compared to sample-scale CNT/NCG transfer and eBeam lithography.

◼ CONCLUSION

We have successfully integrated graphene thermal emitters on photonic waveguides and demonstrated their mid-IR emission into the waveguide and out of a grating coupler. Simulations predict emitter temperatures in the range of 500−900 K,

matching other nanoscale emitter types. We estimate emission coupling efficiencies into the waveguide of up to 68% based on our data, which is favorable over other nanoscale emitters. We have shown operation for at least ∼1 h under ambient conditions. While the PIC in our experiment was mostly characterized for 4.2 μm wavelength targeting CO_2 detection, the integrated graphene thermal emitters radiate in a broad gas absorption "fingerprint" wavelength range of 3−10 μm. This, combined with integrated graphene mid-IR photodetectors, makes them ideal for fully integrated photonic sensors, where the evanescent fields of the waveguides can interact directly with the gaseous environment, enabling ubiquitous gas and environmental sensing.

◼ METHODS

Device Fabrication. The PICs were fabricated from silicon-on-insulator (SOI) substrates with a buried oxide (BOx) layer thickness of $t_{BOx} = 3$ μm and a top silicon (top-Si) thickness of $t_{Top-Si} = 220$ nm. First, 3 μm wide rib waveguides with 50 nm step height were etched into the top-Si by reactive ion etching (RIE), resulting in 170 nm rib height. Two grating couplers per waveguide were included by etching thirty 32 μm long stripes into the top-Si by RIE. The first two stripes were 2.7 and 2.14 μm wide with a distance of 0.56 μm, while the other 28 stripes shared a 2.7 μm period and a 4:6 relation of nonetched to etched width. 40 nm palladium (Pd) contacts were then evaporated and patterned by lift-off. Next, a monolayer of graphene grown by chemical vapor deposition on a copper (Cu) foil was wet-transferred onto the chips using a PMMA-assisted wet-transfer method and patterned with an oxygen (O_2) plasma RIE process. Electrical isolation of the graphene from the top-Si was obtained through the native silicon oxide (SiO_2) on the top-Si. The shallow step height of the rib-waveguide allowed the safe graphene transfer without risking mechanical damage at the steep waveguide edges, which feature ∼88° sidewall angles. Finally, a 40 nm aluminum oxide layer (Al_2O_3) was deposited using atomic layer deposition (ALD) to encapsulate the graphene and patterned by wet-chemical etching.

Waveguide Simulation. The fundamental quasi-TE mode profile in the waveguides was calculated for $\lambda = 4.2$ via the Ansys Lumerical mode solver. The refractive index of Si was taken from the built-in model, while the index of the ALD-deposited Al_2O_3 was measured by spectroscopic ellipsometry. The perfectly matched layer (PML) boundaries were placed sufficiently far to ensure they would not influence the mode profile. The simulation was extended for the wavelength range of the IR camera from 3 to 5 μm and shows single mode behavior above 4.3 μm.

Electro-Thermal Simulation. COMSOL Multiphysics software was used to investigate the electro-thermal behavior of our emitters with finite element simulations. The main focus of the simulation was to investigate the failure modes, such as thermal runaway and breakdown, as observed in the experiment. In both device configurations described in the main text, the graphene sheets were modeled using 2D boundaries with an effective thickness of 1 nm, optimizing the computation time. The substrate temperature was set by defining a fixed temperature boundary at 293 K to the bottom surface of the substrate. Air convection was included in the simulations using a typical 5 W/m²K free convective heat transfer coefficient on the top surfaces of the emitters. In the air gaps underneath the suspended graphene, only the air conduction effect was

considered since the air gap depth was sufficiently small to neglect the air convection effect. The graphene/Si and graphene/Al_2O_3 thermal boundary resistivities were not included in the simulation. Yet, we expect that the significant difference in thermal resistivities of Si and air allows us to accurately predict the "hot spots" located in and near the suspended graphene areas without including the thermal boundaries resistivities. The electrical conductivity of the graphene was set to 6.5×10^5 S/m, based on an average measured resistance of 400 Ω.

ASSOCIATED CONTENT

Supporting Information

The Supporting Information is available free of charge at https://pubs.acs.org/doi/10.1021/acsphotonics.3c01892.

SI1 − Experimental loss extraction using the cutback method (DOC). SI2 − Numerical simulation of the grating coupler performance (DOC). SI3 − IR camera calibration modes and current limitations (DOC). SI4 − Internal efficiency of the entire optical system (DOC). SI5 − Simulation of the grating coupler emission fraction as detected from the IR camera vs wavelength (DOC). SI6 − Quantitative analysis of the estimated emitter emission progression with heating power (DOC). SI7 − Investigation of the possible breakdown mechanisms (DOC) (PDF)

AUTHOR INFORMATION

Corresponding Author

Max C. Lemme − Advanced Microelectronic Center Aachen, AMO GmbH, 52074 Aachen, Germany; Chair of Electronic Devices (ELD), RWTH Aachen University, 52074 Aachen, Germany; orcid.org/0000-0003-4552-2411; Email: max.lemme@rwth-aachen.de

Authors

Nour Negm − Advanced Microelectronic Center Aachen, AMO GmbH, 52074 Aachen, Germany; Chair of Electronic Devices (ELD), RWTH Aachen University, 52074 Aachen, Germany; orcid.org/0000-0001-5659-650X

Sarah Zayouna − Senseair AB, 824 08 Delsbo, Sweden; Department of Applied Physics, KTH Royal Institute of Technology, 114 19 Stockholm, Sweden

Shayan Parhizkar − Advanced Microelectronic Center Aachen, AMO GmbH, 52074 Aachen, Germany; Chair of Electronic Devices (ELD), RWTH Aachen University, 52074 Aachen, Germany; orcid.org/0000-0001-7976-1344

Pen-Sheng Lin − Division of Micro- and Nanosystems, School of Electrical Engineering and Computer Science, KTH Royal Institute of Technology, 100 44 Stockholm, Sweden

Po-Han Huang − Division of Micro- and Nanosystems, School of Electrical Engineering and Computer Science, KTH Royal Institute of Technology, 100 44 Stockholm, Sweden; orcid.org/0000-0002-7659-842X

Stephan Suckow − Advanced Microelectronic Center Aachen, AMO GmbH, 52074 Aachen, Germany; orcid.org/0000-0002-1116-169X

Stephan Schroeder − Senseair AB, 824 08 Delsbo, Sweden

Eleonora De Luca − Senseair AB, 824 08 Delsbo, Sweden

Floria Ottonello Briano − Senseair AB, 824 08 Delsbo, Sweden

Arne Quellmalz − Division of Micro- and Nanosystems, School of Electrical Engineering and Computer Science, KTH Royal Institute of Technology, 100 44 Stockholm, Sweden; orcid.org/0000-0003-3936-818X

Georg S. Duesberg − Institute of Physics, Faculty of Electrical Engineering and Information Technology (EIT 4) & SENS Research Centre, University of the Bundeswehr Munich, 85577 Neubiberg, Germany; orcid.org/0000-0002-7412-700X

Frank Niklaus − Division of Micro- and Nanosystems, School of Electrical Engineering and Computer Science, KTH Royal Institute of Technology, 100 44 Stockholm, Sweden; orcid.org/0000-0002-0525-8647

Kristinn B. Gylfason − Division of Micro- and Nanosystems, School of Electrical Engineering and Computer Science, KTH Royal Institute of Technology, 100 44 Stockholm, Sweden; orcid.org/0000-0001-9008-8402

Complete contact information is available at:
https://pubs.acs.org/10.1021/acsphotonics.3c01892

Notes

The authors declare no competing financial interest.

ACKNOWLEDGMENTS

REFERENCES

(1) Feng, S.; Farha, F.; Li, Q.; Wan, Y.; Xu, Y.; Zhang, T.; Ning, H. Review on Smart Gas Sensing Technology. Sensors 2019, 19 (17), 3760.

(2) Nazemi, H.; Joseph, A.; Park, J.; Emadi, A. Advanced Micro- and Nano-Gas Sensor Technology: A Review. Sensors 2019, 19 (6), 1285.

(3) Liu, X.; Cheng, S.; Liu, H.; Hu, S.; Zhang, D.; Ning, H. A Survey on Gas Sensing Technology. Sensors 2012, 12 (7), 9635−9665.

(4) Hodgkinson, J.; Tatam, R. P. Optical Gas Sensing: A Review. Meas. Sci. Technol. 2013, 24 (1), 012004.

(5) Peng, C.; Qian, K.; Wang, C. Design and Application of a VOC-Monitoring System Based on a ZigBee Wireless Sensor Network. IEEE Sens. J. 2015, 15 (4), 2255−2268.

(6) Xiao, G.; Zhiyi, Z.; Weber, J.; Heping, D.; McIntosh, H.; Desrosiers, D.; Gang, N.; Doyun, W.; Dunford, J.; Tunney, J.; Darcovich, K.; Diaz-Quijada, G. Trace Amount Formaldehyde Gas Detection for Indoor Air Quality Monitoring. In 2011 IEEE International Instrumentation and Measurement Technology Conference; IEEE: Binjiang, 2011; pp 1−4.

(7) Wang, F.; Lin, W.; Liu, Z.; Wu, S.; Qiu, X. Pipeline Leak Detection by Using Time-Domain Statistical Features. IEEE Sens. J. 2017, 17 (19), 6431−6442.

(8) Chen, J.; Gu, J.; Zhang, R.; Mao, Y.; Tian, S. Freshness Evaluation of Three Kinds of Meats Based on the Electronic Nose. Sensors 2019, 19 (3), 605.

(9) Wang, Y.; Tong, M. M.; Zhang, D.; Gao, Z. Improving the Performance of Catalytic Combustion Type Methane Gas Sensors Using Nanostructure Elements Doped with Rare Earth Cocatalysts. Sensors 2010, 11 (1), 19−31.

(10) Harrou, F.; Dairi, A.; Sun, Y.; Kadri, F. Detecting Abnormal Ozone Measurements With a Deep Learning-Based Strategy. *IEEE Sens. J.* **2018**, *18* (17), 7222−7232.

(11) Fine, G. F.; Cavanagh, L. M.; Afonja, A.; Binions, R. Metal Oxide Semi-Conductor Gas Sensors in Environmental Monitoring. *Sensors* **2010**, *10* (6), 5469−5502.

(12) Kanan, S.; El-Kadri, O.; Abu-Yousef, I.; Kanan, M. Semi-conducting Metal Oxide Based Sensors for Selective Gas Pollutant Detection. *Sensors* **2009**, *9* (10), 8158−8196.

(13) Wilson, A. Application of Electronic-Nose Technologies and VOC-Biomarkers for the Noninvasive Early Diagnosis of Gastrointestinal Diseases. *Sensors* **2018**, *18* (8), 2613.

(14) Gordon, I. E.; Rothman, L. S.; Hill, C.; Kochanov, R. V.; Tan, Y.; Bernath, P. F.; Birk, M.; Boudon, V.; Campargue, A.; Chance, K. V.; Drouin, B. J.; Flaud, J.-M.; Gamache, R. R.; Hodges, J. T.; Jacquemart, D.; Perevalov, V. I.; Perrin, A.; Shine, K. P.; Smith, M.-A. H.; Tennyson, J.; Toon, G. C.; Tran, H.; Tyuterev, V. G.; Barbe, A.; Császár, A.; Devi, V. M.; Furtenbacher, T.; Harrison, J. J.; Hartmann, J.-M.; Jolly, A.; Johnson, T. J.; Karman, T.; Kleiner, I.; Kyuberis, A. A.; Loos, J.; Lyulin, O. M.; Massie, S. T.; Mikhailenko, S. N.; Moazzen-Ahmadi, N.; Müller, H.; Naumenko, O. V.; Nikitin, A. V.; Polyansky, O. L.; Rey, M.; Rotger, M.; Sharpe, S. W.; Sung, K.; Starikova, E.; Tashkun, S. A.; Auwera, J. V.; Wagner, G.; Wilzewski, J.; Wcisło, P.; Yu, S.; Zak, E. J. The HITRAN2016 Molecular Spectroscopic Database. *J. Quant. Spectrosc. Radiat. Transfer* **2017**, *203*, 3−69.

(15) Lin, P.-S.; Quellmalz, A.; Huang, P.-H.; Parhizkar, S.; Negm, N.; Suckow, S.; Ottonello-Briano, F.; Lemme, M. C.; Niklaus, F.; Gylfason, K. B. Low-Concentration Detection of CO2 Using Suspended Silicon Waveguides in the Mid-IR. In *CLEO: Science and Innovations*; Optica Publishing Group, 2022; p SF4O-1.

(16) Pi, M.; Zheng, C.; Bi, R.; Zhao, H.; Liang, L.; Zhang, Y.; Wang, Y.; Tittel, F. K. Design of a Mid-Infrared Suspended Chalcogenide/Silica-on-Silicon Slot-Waveguide Spectroscopic Gas Sensor with Enhanced Light-Gas Interaction Effect. *Sens. Actuators, B* **2019**, *297*, 126732.

(17) Jin, T.; Zhou, J.; Lin, H.-Y. G.; Lin, P. T. Mid-Infrared Chalcogenide Waveguides for Real-Time and Nondestructive Volatile Organic Compound Detection. *Anal. Chem.* **2019**, *91* (1), 817−822.

(18) Parhizkar, S.; Prechtl, M.; Giesecke, A. L.; Suckow, S.; Wahl, S.; Lukas, S.; Hartwig, O.; Negm, N.; Quellmalz, A.; Gylfason, K.; Schall, D.; Wuttig, M.; Duesberg, G. S.; Lemme, M. C. Two-Dimensional Platinum Diselenide Waveguide-Integrated Infrared Photodetectors. *ACS Photonics* **2022**, *9* (3), 859−867.

(19) Wang, D.; Madden, S. Designing Absorbers for Graphene Based Mid-Infrared Wide Band Waveguide Photodetectors. *Opt. Express* **2021**, *29* (21), 33850−33863.

(20) Yadav, A.; Agarwal, A. M. Integrated Photonic Materials for the Mid-Infrared. *Int. J. Appl. Glass Sci.* **2020**, *11* (3), 491−510.

(21) Su, P.; Han, Z.; Kita, D.; Becla, P.; Lin, H.; Deckoff-Jones, S.; Richardson, K.; Kimerling, L. C.; Hu, J.; Agarwal, A. Monolithic On-Chip Mid-IR Methane Gas Sensor with Waveguide-Integrated Detector. *Appl. Phys. Lett.* **2019**, *114* (5), 051103.

(22) Huang, L.; Dong, B.; Guo, X.; Chang, Y.; Chen, N.; Huang, X.; Liao, W.; Zhu, C.; Wang, H.; Lee, C.; Ang, K.-W. Waveguide-Integrated Black Phosphorus Photodetector for Mid-Infrared Applications. *ACS Nano* **2019**, *13* (1), 913−921.

(23) Deckoff-Jones, S.; Wang, Y.; Lin, H.; Wu, W.; Hu, J. Tellurene: A Multifunctional Material for Midinfrared Optoelectronics. *ACS Photonics* **2019**, *6* (7), 1632−1638.

(24) Ma, P.; Salamin, Y.; Baeuerle, B.; Josten, A.; Heni, W.; Emboras, A.; Leuthold, J. Plasmonically Enhanced Graphene Photodetector Featuring 100 Gbit/s Data Reception, High Responsivity, and Compact Size. *ACS Photonics* **2019**, *6* (1), 154−161.

(25) Schall, D.; Neumaier, D.; Mohsin, M.; Chmielak, B.; Bolten, J.; Porschatis, C.; Prinzen, A.; Matheisen, C.; Kuebart, W.; Junginger, B.; Templ, W.; Giesecke, A. L.; Kurz, H. 50 GBit/s Photodetectors Based on Wafer-Scale Graphene for Integrated Silicon Photonic Communication Systems. *ACS Photonics* **2014**, *1* (9), 781−784.

(26) Mirza, B. I.; Nash, G. R.; Smith, S. J.; Buckle, L.; Coomber, S. D.; Emeny, M. T.; Ashley, T. Recombination Processes in Midinfrared AlxIn1-xSb Light-Emitting Diodes. *J. Appl. Phys.* **2008**, *104* (6), 063113.

(27) Buss, I. J.; Nash, G. R.; Rarity, J. G.; Cryan, M. J. Three-Dimensional Numerical Modeling of Emission from InSb Light-Emitting Diodes with Patterned Surfaces. *J. Opt. Soc. Am. B* **2008**, *25* (5), 810.

(28) Nash, G. R.; Forman, H. L.; Smith, S. J.; Robinson, P. B.; Buckle, L.; Coomber, S. D.; Emeny, M. T.; Gordon, N. T.; Ashley, T. Mid-Infrared ${\rm Al}_{x}{\rm In}_{1-x}{\rm Sb}$ Light-Emitting Diodes and Photodiodes for Hydrocarbon Sensing. *IEEE Sens. J.* **2009**, *9* (10), 1240−1243.

(29) Cheetham, K. J.; Krier, A.; Marko, I. P.; Aldukhayel, A.; Sweeney, S. J. Direct Evidence for Suppression of Auger Recombination in GaInAsSbP/InAs Mid-Infrared Light-Emitting Diodes. *Appl. Phys. Lett.* **2011**, *99* (14), 141110.

(30) Stephan, S.; Frederic, D.; Markus-Christian, A. Novel InP- and GaSb-Based Light Sources for the near to Far Infrared. *Semicond. Sci. Technol.* **2016**, *31* (11), 113005.

(31) Luo, F.; Fan, Y.; Peng, G.; Xu, S.; Yang, Y.; Yuan, K.; Liu, J.; Ma, W.; Xu, W.; Zhu, Z. H.; Zhang, X.-A.; Mishchenko, A.; Ye, Y.; Huang, H.; Han, Z.; Ren, W.; Novoselov, K. S.; Zhu, M.; Qin, S. Graphene Thermal Emitter with Enhanced Joule Heating and Localized Light Emission in Air. *ACS Photonics* **2019**, *6* (8), 2117−2125.

(32) Miyoshi, Y.; Fukazawa, Y.; Amasaka, Y.; Reckmann, R.; Yokoi, T.; Ishida, K.; Kawahara, K.; Ago, H.; Maki, H. High-Speed and on-Chip Graphene Blackbody Emitters for Optical Communications by Remote Heat Transfer. *Nat. Commun.* **2018**, *9* (1), 1279.

(33) Lawton, L. M.; Mahlmeister, N. H.; Luxmoore, I. J.; Nash, G. R. Prospective for Graphene Based Thermal Mid-Infrared Light Emitting Devices. *AIP Adv.* **2014**, *4* (8), 087139.

(34) Ottonello Briano, F. Mid-Infrared Photonic Devices for on-Chip Optical Gas Sensing. Ph.D. Thesis, KTH Royal Institute of Technology, 2019.

(35) Schröder, S.; Briano, F. O.; Rödjegård, H.; Bryzgalov, M.; Orelund, J.; Gylfason, K. B.; Stemme, G.; Niklaus, F. A Large-Area Single-Filament Infrared Emitter and Its Application in a Spectro-scopic Ethanol Gas Sensing System. *Microsyst. Nanoeng.* **2021**, *7* (1), 87.

(36) Ottonello Briano, F.; Sohlström, H.; Forsberg, F.; Renoux, P.; Ingvarsson, S.; Stemme, G.; Gylfason, K. B. A Sub-Ms Thermal Time Constant Electrically Driven Pt Nanoheater: Thermo-Dynamic Design and Frequency Characterization. *Appl. Phys. Lett.* **2016**, *108* (19), 193106.

(37) Freitag, M.; Chiu, H.-Y.; Steiner, M.; Perebeinos, V.; Avouris, P. Thermal Infrared Emission from Biased Graphene. *Nat. Nano-technol.* **2010**, *5* (7), 497−501.

(38) Kim, Y. D.; Kim, H.; Cho, Y.; Ryoo, J. H.; Park, C.-H.; Kim, P.; Kim, Y. S.; Lee, S.; Li, Y.; Park, S.-N.; Shim Yoo, Y.; Yoon, D.; Dorgan, V. E.; Pop, E.; Heinz, T. F.; Hone, J.; Chun, S.-H.; Cheong, H.; Lee, S. W.; Bae, M.-H.; Park, Y. D. Bright Visible Light Emission from Graphene. *Nat. Nanotechnol.* **2015**, *10* (8), 676−681.

(39) Barnard, H. R.; Zossimova, E.; Mahlmeister, N. H.; Lawton, L. M.; Luxmoore, I. J.; Nash, G. R. Boron Nitride Encapsulated Graphene Infrared Emitters. *Appl. Phys. Lett.* **2016**, *108* (13), 131110.

(40) Junaid, M.; Md Khir, M. H.; Witjaksono, G.; Ullah, Z.; Tansu, N.; Saheed, M. S. M.; Kumar, P.; Hing Wah, L.; Magsi, S. A.; Siddiqui, M. A. A Review on Graphene-Based Light Emitting Functional Devices. *Molecules* **2020**, *25* (18), 4217.

(41) Khasminskaya, S.; Pyatkov, F.; Flavel, B. S.; Pernice, W. H.; Krupke, R. Waveguide-Integrated Electroluminescent Carbon Nano-tubes. *arXiv* **2013**, arXiv:1306.5632.

(42) Fechner, R. G.; Pyatkov, F.; Khasminskaya, S.; Flavel, B. S.; Krupke, R.; Pernice, W. H. P. Directional Couplers with Integrated Carbon Nanotube Incandescent Light Emitters. *Opt. Express* **2016**, *24* (2), 966.

(43) Pyatkov, F.; Fütterling, V.; Khasminskaya, S.; Flavel, B. S.; Hennrich, F.; Kappes, M. M.; Krupke, R.; Pernice, W. H. P. Cavity-Enhanced Light Emission from Electrically Driven Carbon Nanotubes. *Nat. Photonics* **2016**, *10* (6), 420−427.

(44) Khasminskaya, S.; Pyatkov, F.; Słowik, K.; Ferrari, S.; Kahl, O.; Kovalyuk, V.; Rath, P.; Vetter, A.; Hennrich, F.; Kappes, M. M.; Gol'tsman, G.; Korneev, A.; Rockstuhl, C.; Krupke, R.; Pernice, W. H. P. Fully Integrated Quantum Photonic Circuit with an Electrically Driven Light Source. *Nat. Photonics* **2016**, *10* (11), 727−732.

(45) Pyatkov, F.; Khasminskaya, S.; Kovalyuk, V.; Hennrich, F.; Kappes, M. M.; Goltsman, G. N.; Pernice, W. H. P.; Krupke, R. Sub-Nanosecond Light-Pulse Generation with Waveguide-Coupled Carbon Nanotube Transducers. *Beilstein J. Nanotechnol.* **2017**, *8*, 38−44.

(46) Ovvyan, A. P.; Li, M.-K.; Gehring, H.; Beutel, F.; Kumar, S.; Hennrich, F.; Wei, L.; Chen, Y.; Pyatkov, F.; Krupke, R.; Pernice, W. H. P. An Electroluminescent and Tunable Cavity-Enhanced Carbon-Nanotube-Emitter in the Telecom Band. *Nat. Commun.* **2023**, *14* (1), 3933.

(47) Gao, W.; Kono, J. Science and Applications of Wafer-Scale Crystalline Carbon Nanotube Films Prepared through Controlled Vacuum Filtration. *R. Soc. Open Sci.* **2019**, *6* (3), 181605.